Catalysis Science & Technology

ROYAL SOCIETY OF CHEMISTRY

PAPER

View Article Online
View Journal | View Issue

Cite this: *Catal. Sci. Technol.*, 2024, **14**, 903

Cyano-modified poly(triazine imide) with extended π-conjugation for photocatalytic biological cofactor regeneration†

Jianhua Liu,[ab] Jiashu Li,[ab] Fangshu Xing*[b] and Jian Liu *[ab]

Received 10th December 2023,
Accepted 14th January 2024

DOI: 10.1039/d3cy01708g

rsc.li/catalysis

Developing biological cofactor regeneration strategies is crucial for photo-enzyme coupling systems. Here, crystalline poly(triazine imide) (PTI) containing the cyano group (–C≡N) is designed for photocatalytic nicotinamide cofactor oxidation regeneration *via* π–π interaction. The π-conjugation degree and electron delocalization of PTI can be regulated through –C≡N modification. Such a unique extended π-conjugated system promotes the adsorption of the reduced-state nicotinamide cofactor (NADH) on the aromatic skeleton. Moreover, the enhanced charge transfer dynamics expedite the formation of intermediate active species. Accordingly, the optimized conversion rate of NADH to NAD^+ reached 98.2% within 60 min. In contrast, pristine PTI and amorphous polymeric carbon nitride (PCN) gave oxidation yields of 88.1% and 56.8%, respectively. The exclusive selectivity of the oxidized product was further verified by the enzymatic method and nuclear magnetic resonance characterization. This study introduces an innovative method for modulating non-covalent interactions for photo-enzymatic catalysis *via* the extended π-conjugated system.

1. Introduction

Efficient utilization of light energy and its conversion holds paramount significance in optimizing energy structures and promoting sustainable green development. Meanwhile, the biocatalysis system using enzymes as catalysts has many advantages such as high efficiency, greenness, specificity, and selectivity.[1–5] Currently, photo-enzymatic catalysis seamlessly integrates the light absorption capabilities of photocatalysis with the benefits of enzymatic catalysis, including gentle reaction conditions, high activity, and exceptional selectivity.[6–8] As a result, it has emerged as a leading innovation in the realm of artificial photosynthesis.

The nicotinamide cofactor ($NADH/NAD^+$)-based photo-enzyme coupling system is one of the most representative artificial–biological hybrid systems, which can be applied to approximately 90% of the redox catalytic reactions.[6,9] The $NADH/NAD^+$ cofactor acts as the "electron shuttle" to coordinate the electron transfer between enzymes and photocatalysts, enabling selective solar energy conversion through the combination of photocatalytic regeneration and enzymatic catalysis.[10,11] Researchers have been devoted to developing stable and efficient strategies to understand the functioning process of $NADH/NAD^+$ in photo-enzymatic catalysis.[12–16] Inspired by nature, natural enzymes have provided valuable insights into the construction of efficient and sustainable $NADH/NAD^+$ regeneration strategies.[17] Through non-covalent interactions such as hydrogen bonding, ionic bonding, and π–π stacking, the free nicotinamide cofactor can selectively bind to the active site of the biological enzyme.[18,19] This specific interaction is a crucial step in cellular redox processes, ensuring the effective participation of NADH in electron transfer and energy metabolism.[18] Therefore, introducing non-covalent regulation into the semi-artificial photosynthesis involving redox enzymes may also accelerate the cofactor conversion process.[20] For example, surface modification of Au nanoparticles can increase the local concentration of NAD^+ around the nanoparticles through the electrostatic attraction generated by surface ligands, thereby enhancing the electron transfer during NADH regeneration.[21] Additionally, due to the conjugated nature of NAD^+, the tri-*s*-triazine building units in polymer carbon nitride (PCN) structures can interact with the adenine ring in the cofactor through π–π stacking, enabling direct electron transfer from PCN to NAD^+ even without the electron mediator.[20] Therefore, modulating the interactions between the photocatalyst and the $NADH/NAD^+$ can promote their intimate contact, thereby optimizing the electron transfer process and subsequent biosynthesis.[22]

[a] *College of Materials Science and Engineering, Qingdao University of Science and Technology, Qingdao 266042, P. R. China. E-mail: liujian@qibebt.ac.cn*
[b] *Qingdao Institute of Bioenergy and Bioprocess Technology, Chinese Academy of Sciences, Shandong Energy Institute, Qingdao New Energy Shandong Laboratory, Qingdao 266101, P. R. China. E-mail: xingfs@qibebt.ac.cn*

† Electronic supplementary information (ESI) available. See DOI: https://doi.org/10.1039/d3cy01708g

The nicotinamide cofactor contains an aromatic ring in its molecular structure, which endows it with a rich π electron cloud.[23] Regulating the π–π interaction between the photocatalyst and NADH is beneficial for photogenerated charge directional transport and improves the energy conversion efficiency of the photo-enzyme coupling system.[20] PCN is a material composed of carbon and nitrogen elements, where C and N atoms form π bonds by sharing electrons, creating a π electron system.[24,25] Since Wang *et al.* first demonstrated it in 2009, polymeric carbon nitride (PCN) can be used as a non-metallic photocatalyst for photocatalytic hydrogen production, and research on PCN photocatalysts has developed rapidly.[26] For photocatalytic biological cofactor regeneration, the π electron clouds of the tri-*s*-triazine unit in carbon nitride can interact with the adenine moiety in NADH.[20,22] Additionally, PCN has advantages such as chemical stability, biocompatibility, and suitable band positions that satisfy NADH oxidation potential, making it a promising cofactor oxidation photocatalyst.[27] However, the photocatalytic activity of PCN is also severely restricted due to its amorphous structure, many defects in the bulk, and serious carrier recombination. In contrast to PCN, crystalline poly(triazine imide) (PTI) and poly(heptazine imide) (PHI) exhibit a more organized atomic structure and planar formation, leading to the extension of the π-conjugated plane.[5,28,29] This may facilitate π–π stacking interactions with NADH, enhancing its binding and participation in enzymatic reactions. In addition, due to the ordered arrangement of atoms in crystalline carbon nitride, it exhibits higher conductivity and facilitates charge transfer properties. For example, Chang *et al.* copolymerized urea with monomers such as 2-aminothiophene-3-carbonitrile to produce amorphous carbon nitride with enhanced light absorption. Further ionic heat treatment in eutectic salts helps to increase the polymerization degree. Therefore, the H_2-evolution apparent quantum yield of the optimized poly(heptazine imide) reached 12% under 420 nm illumination.[30] Meanwhile, Zhang *et al.* prepared narrow-band gap PHI (N-PHI) with an ordered twisted interface by polycondensation polymerization. The results showed that the enhanced light absorption and the promotion of the carrier separation–transfer greatly improved the photocatalytic performance of N-PHI (AQY = 20% at 450 nm).[31] Therefore, crystalline carbon nitride materials have great potential in promoting photogenerated carrier utilization in NADH regeneration. Furthermore, π–π interactions between crystalline carbon nitride and NADH can be finely tuned by modifying the π-conjugation property. When the surface defects are introduced, such as missing atoms,[32] impurities[33,34] or functionalization,[35,36] additional electronic states could be generated that interact with the existing π-conjugated planes, further enhancing the conjugation of the crystalline carbon nitride.[37] Typically, cyano (–C≡N) is a functional group with strong electronegativity that can influence the electron distribution in carbon nitride through the electron-attracting effect, further extending the π conjugation plane.[32,38] However, we still lack sufficient understanding of the rational construction and the utilization of non-covalent interactions to develop more efficient and biocompatible photo-enzyme coupling systems (Table S1†).

Herein, utilizing the interaction between the adenine subunit of NADH (Fig. 1a) and the electron-rich layered structure through π–π stacking interaction, we first applied PTI for photocatalytic NADH oxidation. The effect of bio-inspired π–π interaction on photo-enzymatic catalysis was systematically explored by comparing it with an amorphous tri-*s*-triazine structure and highly ordered triazine-based framework. It was found that the existence of consecutive π-conjugation is beneficial for biological cofactor adsorption and utilization. Moreover, by treating the as-obtained PTI in H_2/Ar gas mixtures under varying heating conditions, cyano groups (–C≡N) are subtly introduced. The π–π interaction between cyano-modified PTI (D-PTI) and cofactor can be further enhanced by extending the π-conjugated structure, which plays a crucial role in maximizing the regeneration efficiency of cofactors. The ultimate oxidation conversion rate of NADH to NAD^+ over D-PTI can approach close to 100% within 60 minutes, which is 1.1 times higher than that of PTI and 1.73 times higher than that of PCN. Experimental data also proved the fast charge carrier separation and transport in an optimized π-conjugation structure. Ultimately, the dual regulation of the π–π adsorption configuration of the NADH cofactor and charge carrier dynamics of the metal-free conjugate system presents a promising approach to achieve efficient, highly selective, and biocompatible biological cofactor regeneration reactions.

2. Experimental section

2.1. Materials

KCl, NaH_2PO_4, Na_2HPO_4, $Na_2C_2O_4$, $CuCl_2$, and HCOOH were purchased from Sinopharm. Isopropanol (IPA) was obtained from Macklin. L-Tryptophan (TRP), LiCl, and 2,2,6,6-tetramethylpiperidine (HTMP) were purchased from Aladdin. Dicyandiamide (DCDA), reduced-state β-nicotinamide adenine dinucleotide (1,4-NADH), oxidized-state β-nicotinamide adenine

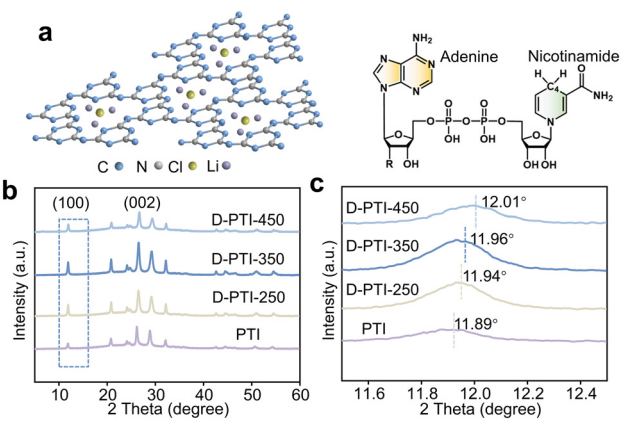

Fig. 1 (a) Structures of PTI and NADH. (b and c) XRD patterns of PTI, D-PTI-250, D-PTI-350, and D-PTI-450.

dinucleotide (NAD^+), and formate dehydrogenase from *Candida boidinii* (FDH, EC.1.2.1.2, F8649) were acquired from Sigma-Aldrich. All chemicals were used without further purification.

2.2. Synthesis of polymer carbon nitride (PCN)

Four grams of dicyandiamide (DCDA) were placed in a porcelain boat and subjected to calcination at 550 °C in a tubular furnace for a duration of 4 h, using a heating rate of 5 °C min^{-1}. The yellow powders were collected and labelled as polymer carbon nitride (PCN).

2.3. Synthesis of poly(triazine imide)

Typically, DCDA (1 g), KCl (5.5 g), and LiCl (4.6 g) eutectic mixture were milled using the agate mortar. Afterward, the mixture was transferred into an ampoule, and heated at 400 °C at a heating rate of 2 °C min^{-1} for 4 h. After naturally cooling to room temperature, the ampoule was vacuumed and then sealed, followed by heating at 550 °C for 24 h at a heating rate of 1 °C min^{-1}. After the reaction, the ampoule was opened. Then, the products and salt mixture were collected and thoroughly washed with deionized water. Finally, the products were obtained by drying at 60 °C overnight. The sample was denoted as PTI for simplicity.

2.4. Synthesis of cyano-modified poly(triazine imide)

The as-obtained PTI (200 mg) was placed into a porcelain boat, which was then heated to 250, 350, or 450 °C at a ramp rate of 5 °C min^{-1} under the hydrogen and argon mixed atmosphere (5% H_2 + 95% Ar). The temperature was maintained for 1 hour to promote the local pyrolysis of PTI. The samples obtained under different temperatures were denoted as D-PTI-250, D-PTI-350, and D-PTI-450, respectively.

2.5. Characterizations

The crystal phase data were obtained using a powder X-ray diffractometer (XRD, Cu Kα irradiation, λ = 1.5406 Å, 40 kV, 40 mA, Rigaku MiniFlex and analyzed by referring to the "powder diffraction file (PDF) database" (International Center for Diffraction Data). The microstructure was analyzed using a JEOL JEM-ARM300F scanning electron microscopy (SEM) and a JEOL JEM-2010 transmission electron microscopy (TEM). Nitrogen adsorption–desorption isotherms were measured on a Micromeritics ASAP 2460 at 77 K. UV–vis diffuse reflectance spectra (DRS) and UV–vis absorption spectra were obtained on a U-3900 HITACHI spectrophotometer with $BaSO_4$ as a reference sample. X-ray photoelectron spectrometry (XPS) tests were performed on a Thermo Fisher Scientific ESCALAB 250Xi instrument. The monochromatic Al Kα was used as the X-ray source, and the binding energy data were calibrated with a C 1s peak position at 284.8 eV. ^{13}C nuclear magnetic resonance (^{13}C NMR) was collected using the Bruker AVANCE NEO 600 Ascend spectrometer. Fourier transform infrared spectroscopy (FT-IR) spectra were obtained on a Bruker VERTEX 70v instrument. Steady-state photoluminescence (PL) spectra were recorded on a SHIMADIU RF-6000 spectrophotometer. Electron paramagnetic resonance (EPR) tests were conducted on a Bruker EMXPLUS spectrometer.

2.6. Photocatalytic oxidation of 1,4-NADH

The photocatalytic oxidation of NADH experiment was carried out in a 3 mL quartz reactor under continuous illumination using a white LED lamp. The reaction system was composed of 1,4-NADH (120 μL, 25 mmol L^{-1}), phosphate buffer solution (PBS) (2.88 mL, 50 mmol L^{-1}, pH 8), and 3 mg of the photocatalyst (PCN, PTI or D-PTI-*x*). Before the light reaction, the reaction system was stirred in the dark for 10 minutes to mix well. A white LED was used for continuous illumination. The sample was collected at regular intervals. The reaction liquid was subsequently centrifuged and analyzed using a UV–vis spectrometer to quantify the absorbance of NADH at 340 nm, facilitating the determination of NADH concentration and the reaction yield. Typically, the molar absorption coefficient (ε) of 1,4-NADH is 6220 M^{-1} cm^{-1}. The thickness of the cuvette for UV–vis light absorption measurements is 1 cm. The cuvette used for UV–vis light absorption measurements had a path length of 1 cm. Before measuring UV-visible light absorption, the solution was diluted 40 times with deionized water to ensure the applicability of the Lambert–Beer law.

2.7. Enzyme assay for the quantitation of regenerated NAD^+

The reaction solution (100 μL) was first mixed with 3.9 mL of phosphate buffer (pH 8.0, 50 mmol L^{-1}), diluting it 40 times. Next, 20 μg FDH and 10 μL HCOONa (10 mmol L^{-1}) were added to the diluted reaction solution. The change in the NADH concentration was monitored using an *in situ* UV–vis spectrometer at 340 nm.

2.8. Photoelectrochemical measurements

Photoelectrochemical measurements were performed using a CHI660 electrochemical workstation. The measurements were conducted with a standard three-electrode system consisting of 0.2 mol L^{-1} Na_2SO_4 as the electrolyte, Pt foil as the counter electrode, and Ag/AgCl (sat. KCl) as the reference electrode. The working electrodes were prepared by dispersing the 20 μL ethanol solution containing 0.04 mg of the catalyst on indium tin oxide (ITO) glass with a target area of 0.5 cm^2. The transient photocurrent and Mott–Schottky (AC frequencies of 0.5, 1, and 1.5 kHz) tests were carried out in 0.2 mol L^{-1} Na_2SO_4 electrolyte. The electrochemical impedance spectrum (EIS) was obtained under 10 mV AC voltage with a frequency range from 0.01 to 100 000 Hz. The electrolyte for the EIS experiment was $K_3[Fe(CN)_6]/K_4[Fe(CN)_6]$/KCl (10 mmol L^{-1}, 10 mmol L^{-1}, 0.5 mmol L^{-1}) mixed solution. The measured potential *vs.* Ag/AgCl (sat. KCl) was converted to the reversible hydrogen electrode (RHE) scale based on the Nernst equation:

$$E_{RHE} = E_{Ag/AgCl} + 0.059 \times pH + E^{\theta}_{Ag/AgCl} \quad (1)$$

where $E^{\theta}_{Ag/AgCl}$ = 0.197 V at 25 °C (2)

3. Results and discussion

3.1. Structure, morphology, and composition analyses

The crystal structure of the as-obtained samples was examined by powder X-ray diffraction (XRD). For PCN samples, two clear (100) and (002) peaks were observed at 13.3 and 27.4° (Fig. S1†).[39] For both PTI and D-PTI samples, it can be observed that all the samples exhibited similar X-ray diffraction characteristics, which are typical diffraction peaks of PTI (Fig. 1b and c).[28] This result indicates that after hydrogen treatment, D-PTI samples still maintained the original crystallinity. Note that, as shown in Fig. 1c, the (100) and (002) planes of the D-PTI samples were significantly shifted to a higher angle than those of the PTI sample. This result reflects that D-PTI after hydrogen treatment exhibits closer interlayer stacking than PTI.[40,41]

From Fig. 2a and S2,† it can be observed that the D-PTI-350 sample exhibits a hexagonal prism morphology. Transmission electron microscopy (TEM) and high-resolution transmission electron microscopy (HRTEM) images (Fig. 2b and c) further reveal the microstructure of the D-PTI-350 sample. The lattice fringes with a distance of 0.72 nm belong to the (100) plane of D-PTI-350, which is slightly smaller than the 0.75 nm of PTI (Fig. S3†). This is consistent with the variation in XRD peaks. The high-angle annular dark field and the corresponding energy dispersive X-ray (EDX) elemental mappings (Fig. 2d–g) confirmed that the D-PTI-350 sample contains uniformly distributed C, N, and Cl elements. The existence of the Li element was not observed during EDX characterization. The specific surface areas of PTI and D-PTI-350 samples were recorded as 48 and 52 $m^2\ g^{-1}$ (Fig. S4†). Further investigation of the chemical composition and local structure of the sample was conducted using XPS analyses. All samples showed C, N, Li, K, and Cl, in good accordance with previous reports (Fig. S6†). The high-resolution C 1s spectra of the PTI and D-PTI-350 are shown in Fig. 3a. The binding energy peaks centered at 284.8 and 288.2 eV obtained from PTI can be attributed to the uncertain carbon from the surrounding environment and N═C–N in typical aromatic heterocycles, respectively.

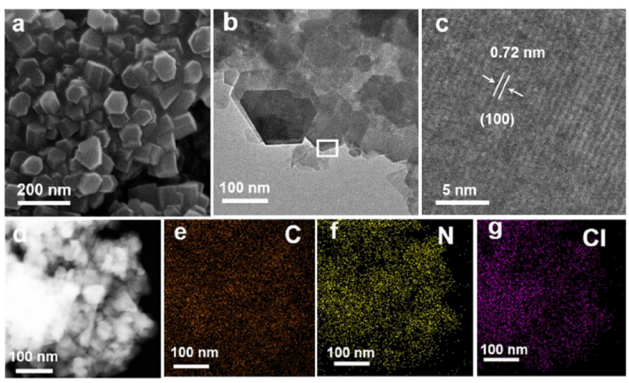

Fig. 2 (a) SEM, (b) TEM, and (c) HRTEM images of D-PTI-350. (d) Dark-field image of D-PTI-350 and corresponding EDX elemental mappings for (e) C, (f) N, and (g) Cl elements, respectively.

From the C 1s spectrum of D-PTI-350, an additional peak centered at 286.4 eV was observed, indicating t the introduction of –C≡N.[42–45] For D-PTI-350, the binding energy peak corresponding to N═C–N appears at 288.2 eV, which is 0.2 eV higher than that observed from PTI because of the electron-withdrawing effect of –C≡N.[46,47] The high-resolved N 1s XPS spectrum of the D-PTI-350 sample can be deconvoluted into two main peaks (Fig. 3b). The main peak of 398.4 eV belongs to the sp^2 hybrid nitrogen of the triazine unit (C═N–C), while the other main peak of 400.0 eV corresponds to the bridging N. Interestingly, the N 1s spectrum of the D-PTI-350 sample shows a decrease in the content of the C═N–C bond (Table S2†). This reduction can be attributed to the cleavage of the C═N–C bond, leading to the formation of –C≡N groups. Based on the above analyses, it can be concluded that by treating PTI with hydrogen, the triazine units were opened and the terminal amino groups in the PTI structure were removed. With the loss of a small number of N atoms, edge defects were introduced into the PTI structure, resulting in the generation of the –C≡N functional groups.[48]

Next, the crystal structures of the PTI and D-PTI-350 samples were characterized by solid-state ^{13}C nuclear magnetic resonance (NMR), as shown in Fig. 3c. The C nucleus is positioned adjacent to the protonation of the bridging nitrogen and protonated triazine nitrogen, leading to chemical shifts at 162 and 158 ppm. The chemical shifts at 168 ppm correspond to the resonance of the C species, neighbouring the non-protonated ring N atoms. These variations in chemical shifts reflect the different chemical environments surrounding the C nucleus.[49] In addition, the D-PTI-350 sample does not show a new nuclear magnetic formant peak, indicating that hydrogen gas treatment does not damage the main molecular structure of the PTI sample. Fourier transform infrared spectroscopy (FT-IR) and electron paramagnetic resonance (EPR) characterization were conducted to investigate the structural variation of D-PTI-350. The FT-IR spectra in Fig. 3d show that the prepared sample contained similar functional groups. For the samples, the strong bands at 808 cm^{-1} are assigned to the breathing mode of the triazine-based units. The peaks in the region of 1200–1600 cm^{-1} can be attributed to the stretching mode of CN heterocycles. The vibrations located at 3200 cm^{-1} are mainly caused by the surface amino vibrations.[5,39] Meanwhile, the D-PTI-350 sample exhibits a typical cyano vibrational peak at 2165 cm^{-1}, which is consistent with the XPS analysis results, further confirming the successful incorporation of the –C≡N functional group in PTI (Fig. 3d and S7 and S8†).[50] This could be attributed to the interaction of hydrogen with the PTI sample during heating, which disrupts a small number of triazine rings within the structure, resulting in the introduction of –C≡N

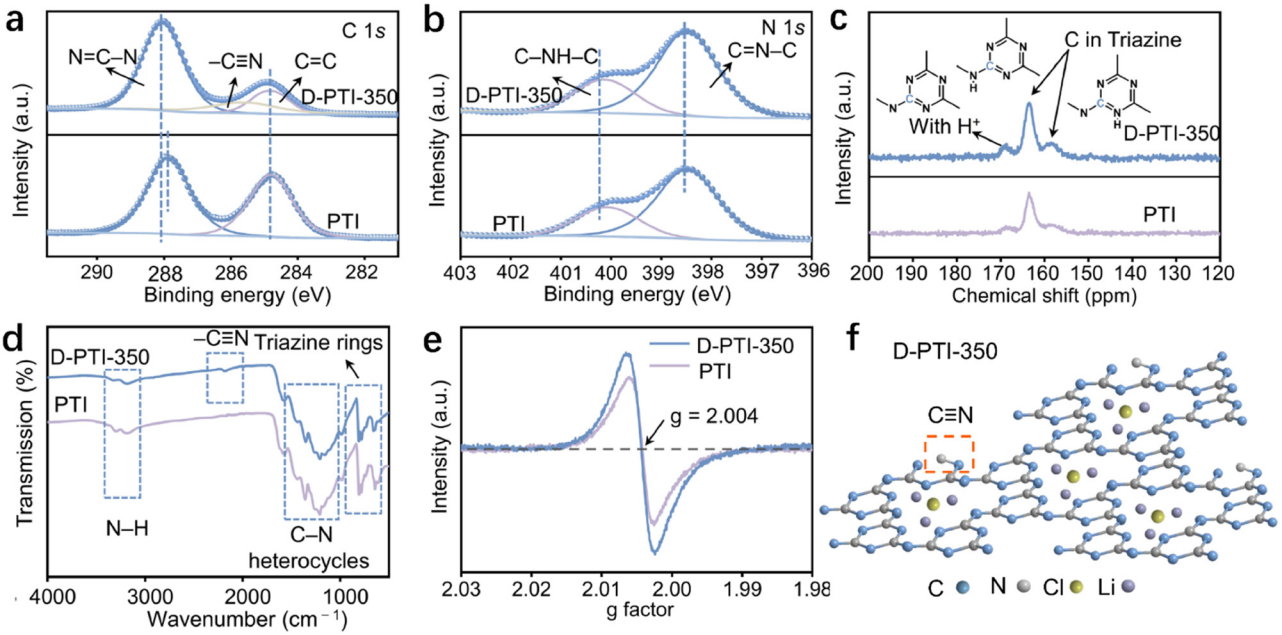

Fig. 3 (a) C 1s, (b) N 1s, (c) ^{13}C NMR, (d) FT-IR, and (e) EPR spectra of PTI and D-PTI-350. (f) Structure diagram of D-PTI-350.

groups. As shown in Fig. 3e, both PTI and D-PTI-350 show the single Lorentzian line with g of 2.004, which is caused by the unpaired (delocalized) electrons in the triazine ring.[51] D-PTI-350 shows a stronger EPR signal than PTI due to the increase in the unpaired electron density caused by cyano modification. The increase in delocalized electron density[52] also indicates the expansion of π conjugated system of the D-PTI-350 sample.[33,53] To sum up, we successfully prepared cyano-modified crystalline carbon nitride with tightly stacked two-dimensional structure and –C≡N group sites in the extended π-conjugation system (Fig. 3f).

3.2. Optical properties and energy band structure analyses

Subsequently, the light absorption and carrier dynamics were studied to understand the enhanced catalytic activity of D-PTI-350. The UV–vis absorption spectra showed that D-PTI-350 has intrinsic absorption band edges similar to PTI, indicating the maintenance of the main triazine structure (Fig. 4a). The absorption band edge at approximately 400 nm in the PTI structure primarily arises from the π–π* electron transition of the sp^2 aromatic series. Besides, a slight change in the absorption tail of D-PTI can be observed. The enhanced absorption tail in the visible light region is probably attributed to the introduction of –C≡N groups.[28] Then, the conduction band (CB) positions are obtained through the Mott–Schottky test. The flat-band potentials of the PTI sample and D-PTI-350 sample are −0.73 and −0.52 V, as shown in Fig. S9 and S10,† respectively. Therefore, the band locations of all the samples are shown in Fig. 4b. The more positive oxidation potential can impart stronger oxidation performance to D-PTI-350 than to PTI.

In addition to the optimization of the energy band structure, cyano groups are expected to boost the separation and transport of photogenerated charge carriers. As shown in Fig. S11,† compared with pristine PTI, the fluorescence intensity of D-PTI-350 undergoes a sharp quenching, indicating that the introduction of the cyano group can effectively suppress the recombination of photogenerated charges.[47,54,55] To obtain more direct evidence of charge mobility of PTI and D-PTI-350, photoelectrochemical measurements were carried out. As shown in the electrochemical impedance spectroscopy (EIS) (Fig. 4c), D-PTI-350 exhibits a much smaller arc radius than PTI, illustrating that D-PTI-350 has better conductivity. This is due to the introduction of trace cyano groups after the heat treatment under the hydrogen atmosphere of PTI, which increases the

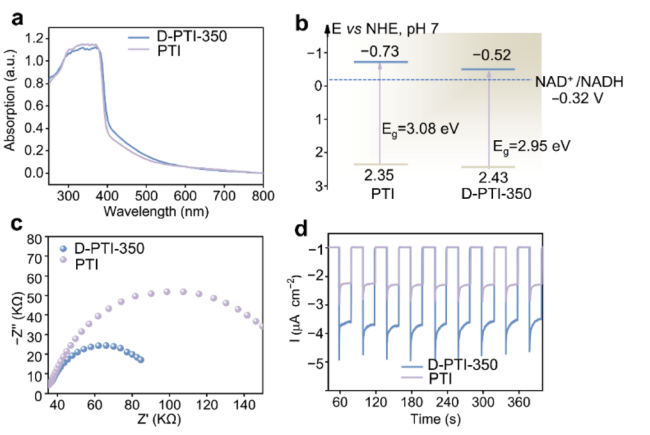

Fig. 4 (a) DRS spectra of PTI and D-PTI-350. (b) Band structure diagrams of PTI and D-PTI-350. (c) EIS spectra and (d) transient photocurrent responses of PTI and D-PTI-350.

electron densities of PTI and improves carrier mobilities.[35] Furthermore, the electronegativity of the cyano group is enough to attract nearby electrons, which improves the electron-supplying ability of the N atom in the D-PTI-350 molecule.[56] In addition, the cyano modification also promotes the electron transport rate by optimizing the crystal structure of D-PTI-350, such as reducing the lattice constant and increasing the crystal packing degree. Therefore, although PTI and D-PTI-350 have the same structure, EIS spectra still show obvious changes due to the introduction of a small amount of cyanide groups. Consistent with the EIS results, D-PTI-350 also exhibited a more sensitive photocurrent response than PTI under transient photocurrent measurements (Fig. 4d). The time-resolved PL decay spectra (TRPL) were collected to provide more information about the carrier average lifetimes. The average carrier lifetime in PTI is 8.54 ns, while that in D-PTI-350 increases to 11.03 ns. The extended lifetimes of photo-generated charges can lead to photoelectrons accumulating on the surface, which is more conducive to the regeneration of the cofactor (Fig. S12, Table S3†).[57] Therefore, it is evident that after introducing the cyano group into PTI, the obtained D-PTI-350 exhibits better charge separation and transfer ability.

3.3. Photocatalytic performances

Considering the expansion of light absorption, the appropriate electronic band structure, and enhanced photo-induced carrier separation and transfer efficiency, we applied D-PTI-350 to study the regeneration performance of NAD^+. The typical photocatalytic process of NAD^+ oxidation regeneration is presented in Fig. 5a. For cyano-riched D-PTI-350, with the extension of time, the absorbance of the reaction system gradually decreases, indicating that NADH is consumed during this process (Fig. 5b). Similar situations were observed using PCN, PTI, D-PTI-250, and D-PTI-450 (Fig. S13†), but the conversion rate dropped. In detail, the NADH consumptions for D-PTI-250, D-PTI-350, D-PTI-450, PTI, and PCN were 91.2, 98.2, 90.8, 88.1, and 58.6%, respectively (Fig. 5c). Moreover, the initial conversion rate of NADH oxidation catalyzed by D-PTI-350 was the highest, reaching 67.5% in 10 minutes. For the apparent quantum efficiency (AQY) test, the D-PTI-350 sample had the highest AQY of 8.4% at 365 nm (Fig. S14†). To more directly compare NADH oxidation rates among PCN, PTI, and D-PTI samples, we calculated the corresponding oxidation reaction rate constants (Fig. S15†). The photocatalytic oxidation curves of NADH over PCN, PTI, and D-PTI samples were fitted using the first-order reaction kinetic equation $\ln(C_t/C_0) = -kt$ (k: rate constant, min^{-1}; C_0: initial concentration of NADH; and C_t: actual NADH concentration). As shown in Fig. S15b,† it can be found that the oxidation rate of D-PTI-350 is 4.7 times and 1.7 times higher than that of PCN and PTI samples. The catalytic selectivity was further analyzed using NMR and enzymatic tests (Fig. 5d and S16 and S17†). As shown in Fig. 5 and S16,† the ^1H NMR spectrum of the commercial NADH substrate exhibits the characteristic signal at 6.79 ppm (C2 position in nicotinamide unite). After the reaction of photocatalytic NADH oxidation over PTI and D-PTI-350, the typical NMR responses assigned to NADH disappeared, demonstrating that the NADH substrate was completely transformed. Correspondingly, the appearance of the new signals at δ = 8.77, 9.10, and 9.28 ppm corresponding

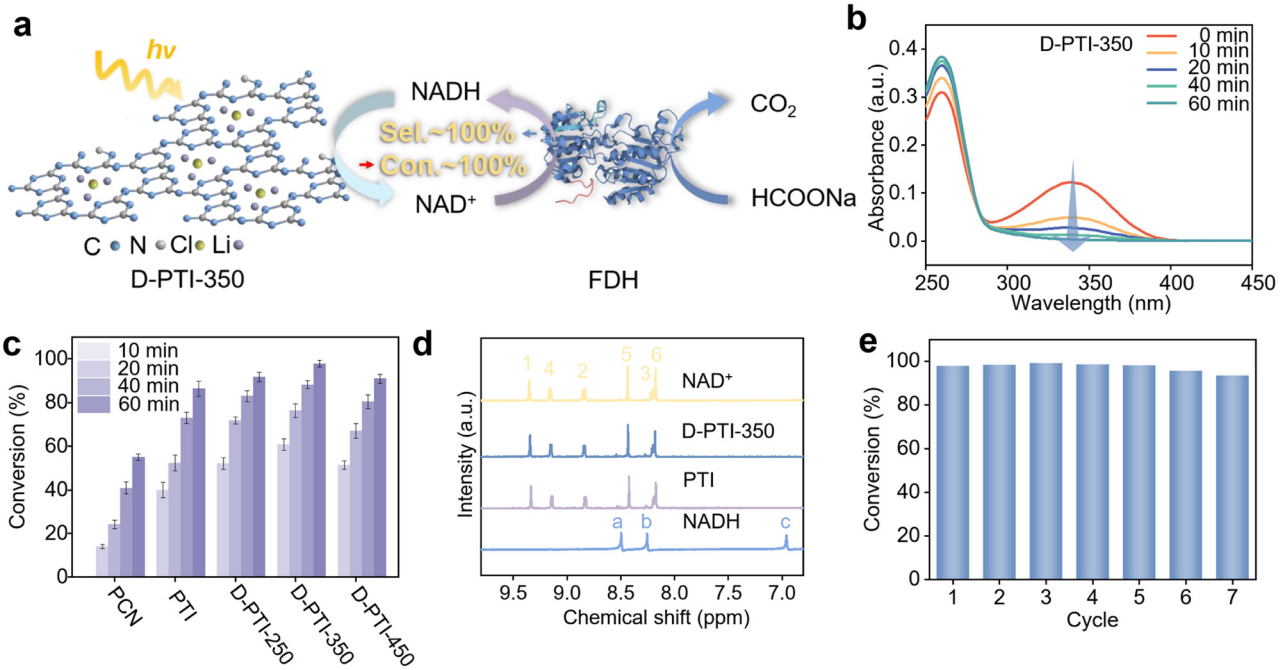

Fig. 5 (a) Schematic illustration of the photocatalytic oxidation of NADH by D-PTI-350. (b) UV–vis absorbance spectra of NAD^+ regeneration of D-PTI-350. (c) Comparison of the conversion rates of NADH oxidation by different catalysts. (d) ^1H NMR (600 MHz, DMSO-d_6) of the reaction product of D-PTI-350 and PTI. (e) Stability test of photocatalytic NADH oxidation over D-PTI-350.

to the nicotinamide group in the oxidized cofactor illustrates the selective formation of NAD^+ products.[14] The oxidized product catalyzed by D-PTI-350 presents a similar NMR signal with commercialized NAD^+, suggesting that the photooxidation of NADH is effectively converted into NAD^+ with enzymatic activity, and no other by-products were generated (Fig. 5d).[15] The enzymatic regeneration of NADH is shown in Fig. S16,† and the nearly 100% reduction in the regeneration efficiency is consistent with the findings from the NMR analyses. The effects of the catalyst concentration, pH, and light source on the oxidation performance of NADH were also investigated (Fig. S18–S20†). The results show that under white light irradiation at 3 mg and pH 8, the catalytic performance was optimal, achieving a conversion rate of nearly 100% within 60 minutes. Furthermore, the catalytic cycling stability of D-PTI-350 was evaluated under these conditions (Fig. 5e). After multiple cycles, the NADH conversion rate remained above 94%, indicating the excellent catalytic durability of D-PTI-350. XRD, FT-IR, and XPS data on D-PTI-350 before and after the photocatalytic reaction revealed no noticeable changes, indicating the strong stability of D-PTI-350 during the catalytic oxidation process (Fig. S21 and S22†).

3.4. π–π stacking analysis and reaction mechanism analysis

The modulation of non-covalent interactions, such as π–π stacking interactions between conjugated photocatalysts and NADH molecules, opens up new possibilities for engineering photocatalytic cofactor regeneration systems. To investigate the strong correlation between NADH and D-PTI-350, we conducted adsorption experiments to verify their interaction. After 24 h of stirring in the dark, the residual NADH in the solution was found to be at least 83.9% for D-PTI-350, while PTI and PCN exhibited residual NADH levels of 90.2% and 97.8%, respectively (Fig. 6a). Additionally, a blank experiment without the catalyst was conducted. There was no decrease in the absorbance of NADH in the solution, which confirmed the presence of π–π interactions between D-PTI-350 and NADH. In addition, we stirred D-PTI-350 and NADH in distilled water at room temperature for 48 h. The obtained suspension was then centrifuged, washed, and dried to remove physically adsorbed NADH on D-PTI-350. Finally, the D-PTI-350/NADH composite was obtained. Element detection was then performed as depicted in Fig. S17.† In the XPS spectrum of the NADH/D-PTI-350 composite material, the peak at 134.0 eV is attributed to phosphorus atoms (P 2p) (Fig. 6b and S23†), indicating the attachment of NADH to D-PTI-350.[58] Therefore, the enhanced conversion rate can be attributed to the strong π–π interaction between the adenine ring of NADH and the PTI moiety with its extended π conjugated structure.

To gain a better understanding of the oxidation reaction process, we conducted a series of active species trapping experiments to investigate the mechanism of NADH oxidation

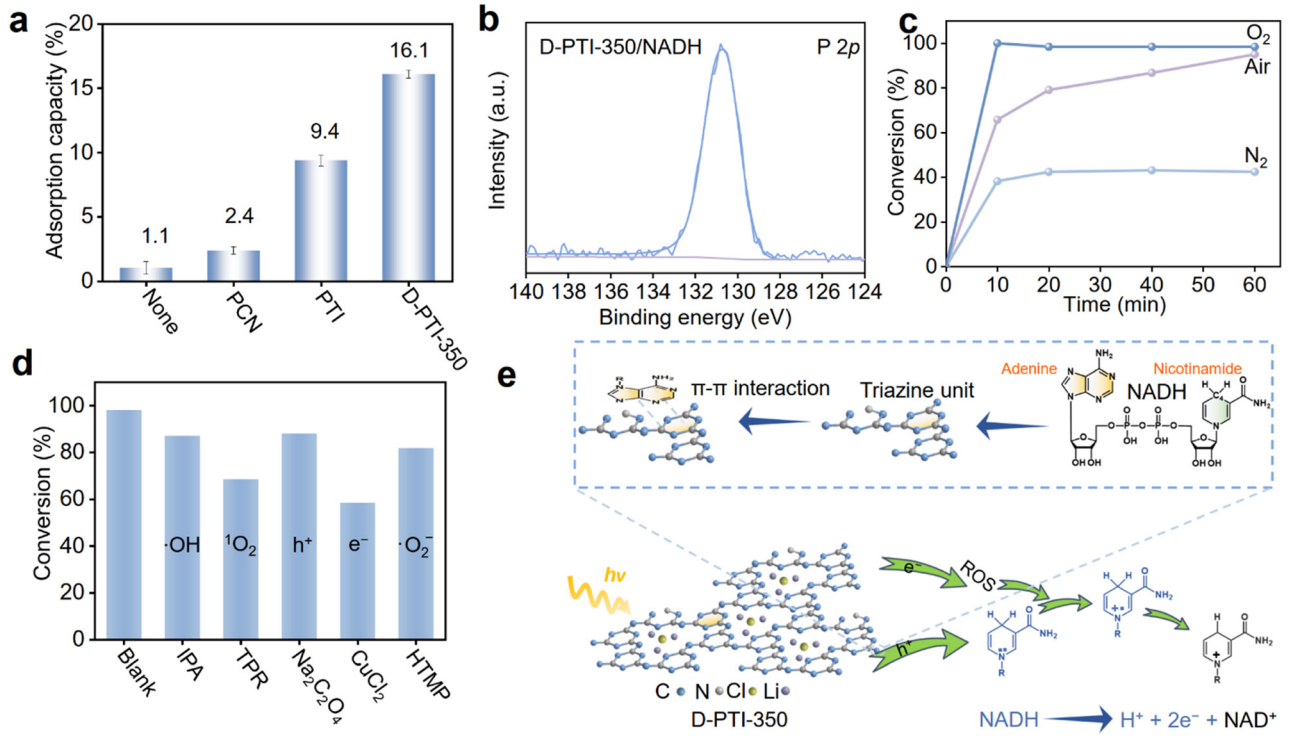

Fig. 6 (a) Comparison of NADH adsorption capacities under dark conditions (24 h). (b) Highly-resolved P 2p spectrum of D-PTI-350 after adsorption of NADH. (c) Photocatalytic NADH oxidation kinetics curves of D-PTI-350 samples under different atmospheres. (d) Effects of different quenching agents on photocatalytic NADH oxidation performance of D-PTI-350. (e) Mechanism diagram of photocatalytic NADH oxidation by D-PTI-350.

catalyzed by D-PTI-350. To clarify the role of molecular oxygen in the reaction, the control experiment was performed in the absence of oxygen. The results showed that the conversion rate of NADH decreased to 56% after 60 minutes (Fig. 6c), indicating the essential role of molecular oxygen in the reaction process. Furthermore, we employed various substances, namely IPA, TRP, $Na_2C_2O_4$, $CuCl_2$, and HTMP, to selectively remove reactive species such as hydroxyl radical ($^{\bullet}OH$), singlet oxygen ($^1O_2$), holes (h^+), electron (e^-), and superoxide radical ($^{\bullet}O^{2-}$), respectively.[59,60] This allowed us to investigate the specific contributions of these reactive species to the overall reaction. As depicted in Fig. 6d, the impact of $^{\bullet}OH$ on the oxidation of NADH can be disregarded. However, the removal of the photogenerated electrons, $^{\bullet}O^{2-}$ radical, and $^1O_2$ species significantly reduces the conversion rate of NADH, indicating their crucial role in the oxidation processes. Based on these findings, a plausible mechanism is proposed, as depicted in Fig. 6e. Initially, NADH was oxidized by photogenerated holes in D-PTI-350, leading to the formation of a corresponding cation radical. Simultaneously, dissolved O_2 molecules in water are reduced by photogenerated electrons to form various reactive oxygen species (ROS). Typically, the active $^{\bullet}O^{2-}$ radicals and $^1O_2$ prefer to extract protons from NADH cation radicals, resulting in the generation of NAD^+.[14,15]

4. Conclusion

In conclusion, cyano-modified crystalline carbon nitride with an extended π-conjugated system was successfully prepared using a two-step pyrolysis method. The extended π-conjugated property increases the oxidation regeneration rate of NADH from 88.1% for PTI to 98.2% for D-PTI-350. More importantly, all the oxidized products were identified as enzymatically active NAD^+. Adsorption experiments have shown that π–π packing interactions occur between NADH molecules and D-PTI-350 substrates, which can promote charge transfer and thus contribute to high reactivity. In addition, free-radical scavenging experiments revealed the dominant role of photoinduced holes and reactive oxygen species in the photocatalytic NADH oxidation process. In summary, the synergistic effect between the extended π-conjugated system and the non-covalent π–π stacking based on the conjugated polymer was found to have a substantial impact on the catalytic properties of biological cofactor regeneration. The thoughtful design of the π-conjugated systems may serve as an inspiration for further advancements in cofactor-dependent photo-enzymatic catalysis.

Author contributions

Jianhua Liu: conceptualization, investigation, validation, formal analysis, writing-original draft. Jiashu Li: validation, formal analysis. Fangshu Xing: conceptualization, investigation, formal analysis, supervision, writing-review and editing. Jian Liu: conceptualization, investigation, formal analysis, supervision, writing-review and editing, funding acquisition.

Conflicts of interest

The authors declare that they have no known competing financial interests or personal relationships that could have appeared to influence the work reported in this paper.

Acknowledgements

The authors are grateful for the support from the National Natural Science Foundation of China (21902082), the Natural Science Foundation of Shandong Province (ZR2019JQ05), the Key Basic Research Project of the Natural Science Foundation of Shandong Province (ZR2019ZD47), the Education Department of Shandong Province (2019KJC006) and the Original Innovation Project of Qingdao City (19-6-2-72-cg).

Notes and references

1 S. Wu, R. Snajdrova, J. C. Moore, K. Baldenius and U. T. Bornscheuer, *Angew. Chem., Int. Ed.*, 2021, **60**, 88–119.
2 F. Hollmann, D. J. Opperman and C. E. Paul, *Angew. Chem., Int. Ed.*, 2021, **60**, 5644–5665.
3 J. Dong, E. Fernández Fueyo, F. Hollmann, C. E. Paul, M. Pesic, S. Schmidt, Y. Wang, S. Younes and W. Zhang, *Angew. Chem., Int. Ed.*, 2018, **57**, 9238–9261.
4 X. Ma, A. C. Hortelao, T. Patino and S. Sanchez, *ACS Nano*, 2016, **10**, 9111–9122.
5 Q. Wang, G. Zhang, W. Xing, Z. Pan, D. Zheng, S. Wang, Y. Hou and X. Wang, *Angew. Chem.*, 2023, **135**, e202307930.
6 S. Zhang, S. Liu, Y. Sun, S. Li, J. Shi and Z. Jiang, *Chem. Soc. Rev.*, 2021, **50**, 13449–13466.
7 W. Harrison, X. Huang and H. Zhao, *Acc. Chem. Res.*, 2022, **55**, 1087–1096.
8 J. Kim and C. B. Park, *Trends Chem.*, 2023, **5**, 133–146.
9 S. H. Lee, D. S. Choi, S. K. Kuk and C. B. Park, *Angew. Chem., Int. Ed.*, 2018, **57**, 7958–7985.
10 W. Dong and J. Liu, *Sci. China: Chem.*, 2023, DOI: **10.1007/s11426-023-1687-2**.
11 W. Wang and J. Liu, *Adv. Energy Sustainability Res.*, 2022, **4**, 2200172.
12 G. Lin, Y. Zhang, Y. Hua, C. Zhang, C. Jia, D. Ju, C. Yu, P. Li and J. Liu, *Angew. Chem., Int. Ed.*, 2022, **61**, e202206283.
13 N. Zhang, S. Trepout, H. Chen and M. H. Li, *J. Am. Chem. Soc.*, 2023, **145**, 288–299.
14 W. Wei, F. Mazzotta, I. Lieberwirth, K. Landfester, C. T. J. Ferguson and K. A. I. Zhang, *J. Am. Chem. Soc.*, 2022, **144**, 7320–7326.
15 S. Zhang, J. Shi, Y. Chen, Q. Huo, W. Li, Y. Wu, Y. Sun, Y. Zhang, X. Wang and Z. Jiang, *ACS Catal.*, 2020, **10**, 4967–4972.
16 P. Singh, R. K. Yadav, K. Kumar, Y. Lee, A. K. Gupta, K. Kumar, B. C. Yadav, S. N. Singh, D. K. Dwivedi, S. H. Nam, A. P. Singh and T. W. Kim, *Catal. Sci. Technol.*, 2021, **11**, 6401–6410.
17 L. Zhao, J. Cai, Y. Li, J. Wei and C. Duan, *Nat. Commun.*, 2020, **11**, 2093.

18 L. Sellés Vidal, C. L. Kelly, P. M. Mordaka and J. T. Heap, *Biochim. Biophys. Acta*, 2018, **1866**, 327–347.
19 A. Zhang, X. Zhuang, J. Liu, J. Huang, L. Lin, Y. Tang, S. Zhao, R. Li, B. Wang, B. Fang and W. Hong, *Nat. Catal.*, 2023, **6**, 266–275.
20 J. Liu and M. Antonietti, *Energy Environ. Sci.*, 2013, **6**, 1486–1493.
21 S. Roy, V. Jain, R. K. Kashyap, A. Rao and P. P. Pillai, *ACS Catal.*, 2020, **10**, 5522–5528.
22 Y. Zhang, Y. Zhao, R. Li and J. Liu, *Sol. RRL*, 2020, **5**, 2000339.
23 X. Wang, T. Saba, H. H. Yiu, R. F. Howe, J. A. Anderson and J. Shi, *Chem*, 2017, **2**, 621–654.
24 W. J. Ong, L. L. Tan, Y. H. Ng, S. T. Yong and S. P. Chai, *Chem. Rev.*, 2016, **116**, 7159–7329.
25 M. Majdoub, Z. Anfar and A. Amedlous, *ACS Nano*, 2020, **14**, 12390–12469.
26 X. Wang, K. Maeda and A. Thomas, *Nat. Mater.*, 2009, **8**, 76–80.
27 D. Zhu, M. Zhang, C. Wang, P. Gai and F. Li, *Chem. Mater.*, 2022, **34**, 11072–11080.
28 M. Liu, C. Wei, H. Zhuzhang, J. Zhou, Z. Pan, W. Lin, Z. Yu, G. Zhang and X. Wang, *Angew. Chem., Int. Ed.*, 2021, **61**, e202113389.
29 Y. Li, B. Li, D. Zhang, L. Cheng and Q. Xiang, *ACS Nano*, 2020, **14**, 10552–10561.
30 M. Chang, Z. Pan, D. Zheng, S. Wang, G. Zhang, M. Anpo and X. Wang, *ChemSusChem*, 2023, **16**, e202202255.
31 J. Zhang, G. Ye, C. Zhang, Z. Pan, S. Wang, G. Zhang and X. Wang, *ChemSusChem*, 2022, **15**, e202201616.
32 H. Lan, Q. Tang, Z. Hou, K. Zhu, X. An, H. Liu and J. Qu, *ACS EST Engg.*, 2023, **3**, 580–589.
33 T. Huo, G. Ba, Q. Deng, F. Yu, G. Wang, H. Li and W. Hou, *Appl. Catal., B*, 2021, **287**, 119995.
34 Q. Li, L. Zhang, J. Liu, J. Zhou, Y. Jiao, X. Xiao, C. Zhao, Y. Zhou, S. Ye, B. Jiang and J. Liu, *Small*, 2021, **17**, 2006622.
35 M. Ai, L. Pan, Y. Chen, C. Shi, Z. F. Huang, X. Zhang and J. J. Zou, *J. Catal.*, 2023, **418**, 22–30.
36 Z. Zhai, H. Zhang, F. Niu, P. Liu, J. Zhang and H. Lu, *ACS Nano*, 2022, **16**, 21002–21012.
37 J. Yang, H. Wang, L. Jiang, H. Yu, Y. Zhao, H. Chen, X. Yuan, J. Liang, H. Li and Z. Wu, *Chem. Eng. J.*, 2022, **427**, 130991.
38 T. Huang, R. Wang, J. Zhang, J. Wang, H. Ge, J. Ren and Z. Zheng, *Chem. Eng. J.*, 2023, **467**, 143469.
39 T. Y. Ma, S. Dai, M. Jaroniec and S. Z. Qiao, *Angew. Chem., Int. Ed.*, 2014, **53**, 7281–7285.
40 Y. Noda, C. Merschjann, J. Tarabek, P. Amsalem, N. Koch and M. J. Bojdys, *Angew. Chem., Int. Ed.*, 2019, **58**, 9394–9398.
41 T. Zhao, Q. Zhou, Y. Lv, D. Han, K. Wu, L. Zhao, Y. Shen, S. Liu and Y. Zhang, *Angew. Chem., Int. Ed.*, 2020, **59**, 1139–1143.
42 Y. Zhao, Z. Liu, W. Chu, L. Song, Z. Zhang, D. Yu, Y. Tian, S. Xie and L. Sun, *Adv. Mater.*, 2008, **20**, 1777–1781.
43 Y. Yang, S. Wang, Y. Jiao, Z. Wang, M. Xiao, A. Du, Y. Li, J. Wang and L. Wang, *Adv. Funct. Mater.*, 2018, **28**, 1805698.
44 G. Liu, Z. Tang, X. Gu, N. Li, H. Lv, Y. Huang, Y. Zeng, M. Yuan, Q. Meng, Y. Zhou and C. Wang, *Appl. Catal., B*, 2022, **317**, 121752.
45 W. Wang, H. Zhang, S. Zhang, Y. Liu, G. Wang, C. Sun and H. Zhao, *Angew. Chem., Int. Ed.*, 2019, **58**, 16644–16650.
46 H. Yu, R. Shi, Y. Zhao, T. Bian, Y. Zhao, C. Zhou, G. I. N. Waterhouse, L. Z. Wu, C. H. Tung and T. Zhang, *Adv. Mater.*, 2017, **29**, 1605148.
47 J. Fu, B. Zhu, C. Jiang, B. Cheng, W. You and J. Yu, *Small*, 2017, **13**, 1603938.
48 W. Ren, J. Cheng, H. Ou, C. Huang, M. M. Titirici and X. Wang, *ChemSusChem*, 2019, **12**, 3257–3262.
49 M. B. Mesch, K. Barwinkel, Y. Krysiak, C. Martineau, F. Taulelle, R. B. Neder, U. Kolb and J. Senker, *Chem. – Eur. J.*, 2016, **22**, 16878–16890.
50 L. Lin, H. Ou, Y. Zhang and X. Wang, *ACS Catal.*, 2016, **6**, 3921–3931.
51 W. Tu, Y. Xu, J. Wang, B. Zhang, T. Zhou, S. Yin, S. Wu, C. Li, Y. Huang, Y. Zhou, Z. Zou, J. Robertson, M. Kraft and R. Xu, *ACS Sustainable Chem. Eng.*, 2017, **5**, 7260–7268.
52 J. Cao, W. Nie, L. Huang, Y. Ding, K. Lv and H. Tang, *Appl. Catal., B*, 2019, **241**, 18–27.
53 K. Li and W. D. Zhang, *Small*, 2018, **14**, e1703599.
54 M. Zhou, P. Yang, R. Yuan, A. M. Asiri, M. Wakeel and X. Wang, *ChemSusChem*, 2017, **10**, 4451–4456.
55 G. Zhang, G. Li, T. Heil, S. Zafeiratos, F. Lai, A. Savateev, M. Antonietti and X. Wang, *Angew. Chem., Int. Ed.*, 2019, **58**, 3433–3437.
56 R. Tang, H. Zeng, Y. Deng, S. Xiong, L. Li, Z. Zhou, J. Wang and L. Tang, *Appl. Catal., B*, 2023, **336**, 122918.
57 P. Zhang, W. Dong, Y. Zhang, L.-N. Zhao, H. Yuan, C. Wang, W. Wang, H. Wang, H. Zhang and J. Liu, *Chin. J. Catal.*, 2023, **54**, 188–198.
58 H. Zhou, Z. Zhang, P. Yu, L. Su, T. Ohsaka and L. Mao, *Langmuir*, 2010, **26**, 6028–6032.
59 Z. Zhang, W. Liu, Y. Zhang, J. Bai and J. Liu, *ACS Catal.*, 2020, **11**, 313–322.
60 C. T. J. Ferguson, N. Huber, K. Landfester and K. A. I. Zhang, *Angew. Chem., Int. Ed.*, 2019, **58**, 10567–10571.